UDC 539.5:661.657

E. Kishor, N. Swaminathan*
Department of Mechanical Engineering,
Indian Institute of Technology Madras, Chennai-600036, India
**n.swaminathan@iitm.ac.in*

A molecular dynamics based comparison of the mechanical properties of three polytypes of cubic BC_3

In this work molecular dynamics simulations are employed to compare the mechanical properties and hardness of three polytypes of cubic BC_3. Firstly, two interatomic Tersoff potentials, with different parameterizations, were identified from the literature for the boron–carbon system. Based on cohesive energies and structural properties from existing ab-initio studies, the suitability of the two potentials for predicting the properties of BC_3 was analyzed. Secondly, using the better interatomic potential, more detailed molecular dynamics simulations were conducted to estimate and compare the elastic, yield, post-yield behavior and hardness of the three polytypes. The elastic constants compare well with existing ab-initio values and vary by at most by 15 % amongst the three polytypes. Response to indentation showed considerable qualitative differences in yield and post-yield response. One of the polytypes showed lower yield strength and seemed more ductile than the other two. The hardness also showed a complex dependence on both the material and the indentation depths. A peculiar, indenter-size dependent pile-up behavior was also seen. Specifically, for lower radii, pile-up was seen on indentation. As the radius of the indenter was increased, pile-up was seen only on retracting the indenter. The higher volume occupied by the indentation-amorphized material was found to be the reason for pile-up on retracting the indenter.

***Keywords**: superhard materials, elastic constants, hardness, molecular dynamics, boron-doped diamond.*

INTRODUCTION

Any material with hardness above 40 GPa is considered as a superhard material. Diamond is the hardest material and is often used for mechanical machining [1]. One of the disadvantages of using diamond is that it reacts with iron at higher temperature and loses its hardness. Therefore, both computational as well as experimental research have focused on developing alternate superhard materials

with better chemical stability based on a combination of elements like B, C, N and O. Boron- based materials are particularly interesting because of boron's capacity to form electron deficient bonding with different elements [2]. Superhard materials like B_6O [3], cubic-BN [4], BC_2N, BC_4N [5] and some of the boron-doped diamonds (BDD) have already been synthesized. BDD like BC_3 [6] and BC_5 [7] can be synthesized from a graphite precursor by direct transformation at high pressure and temperature. BDD are *p*-type semiconductors [8], and are also known to be superconducting [9]. Most importantly, they showed better chemical stability when compared to diamond [10]. One of the critical issues concerning BDD is that the site occupancies of B and C in the crystal structure is not clear, although the stoichiometry is well known. This difficulty arises due to the fact that both B and C have similar atomic radii [11], due to which X-ray diffraction studies are unable to pinpoint the exact locations of B and C. Since boron can substitute carbon atoms in diamond with very little lattice distortion [12], the boron content that can be added is also a subject of extensive research. Thus, several researches based on ab-initio calculations have tried to find the optimum crystal structure and mechanical properties like elastic constants and hardness of various BDD [11–21].

Ab-initio calculations are very accurate, they can be used to study material properties only when at most a few hundred atoms are sufficient. Increasing the number of atoms becomes computationally prohibitive, making it impossible to carry out ab-initio simulations of processes which need a larger number of atoms. For example, simulations to study indentation responses [22] or displacement cascade simulations [23] need several thousands to millions of atoms to obtain meaningful results. Molecular dynamics (MD) simulations, on the other hand, use empirical potentials, making it possible to explore material behavior which needs larger system sizes. Experimental and ab-initio studies have shown BDD to have excellent mechanical and superconducting properties. In order to understand other properties of BDD, it is important to explore the possibility of using MD simulations on BDD. Only one work thus far seems to have considered MD simulations to study BDD (BC_3) [24].

The current work aims to employ MD to compare the mechanical properties like elastic constants and hardness of three polytypes of BC_3. While some ab-initio related works are available for these polytypes, no detailed MD simulations have been carried out. Two aspects are important for successfully conducting MD simulations, (a) the basic crystal structure of the material being studied and (b) the interatomic potential. Considering the structure, several configurations for BC_3 have been predicted over the years using ab-initio methods. For example, Lowther [12] predicted two structures for BC_3. Both were tetragonal with one having an 11 % difference between the lattice constant and the other having 3 % difference. One of the structures of BC_3 reported in [12] was cubic. MD simulation was conducted on BC_3 by Nkambule et al. [24], they reported a tetragonal unit cell with the lattice constant differing by less than 3 %. They also found elastic constants for BC_3 by considering it to be cubic using MD simulation. Reference [13] reported a tetragonal *P*-42*m*, while [14] found the following three low energy structures, (a) orthorhombic *Pmma-a*, (b) orthorhombic *Pmma-b*, (c) tetragonal *P*-4*m*2 for BC_3. Yang et al. [21] conducted tensile tests on nearly cubic structure of BC_3 in different directions of the unit cell. They concluded that it is metallic at equilibrium and remains so under large strains, which makes it the hardest conductor. In 2013 another structure with space group *R*3*m* was reported [11]. Zhang et al. [19], claimed to have solved the crystal structure of BC_3 using an unbiased swarm structure search and predicted the structure to be cubic with space group *I*-43*m*. More

recently, BC_3 is predicted to have monoclinic structure with space group $C2/m$ [15]. Other than the work in [24], where the authors calculated elastic constants, all the other computational works on BC_3 are based on ab-initio calculations.

It is thus clear from the above survey that several structures, with different symmetries, have been proposed for BC_3 using ab-initio calculations. It is now instructive to ask which one is the correct structure? To answer this question we consider the experimental synthesis of BC_3 in 2012 [6] which clearly established BC_3 to have cubic symmetry using electron energy loss spectroscopy. Since the experimentally determined structure is cubic, we believe BC_3 has a cubic symmetry. However, since there seems to be three possible cubic structures, BC_3 (a) from [24], BC_3 (b) from [12] and one from [19] (called BC_3 (c) in this work), we will consider all these three structures and examine their behavior using existing interatomic potentials. Of all the three structures, the one proposed in [19] seems to be the most accurate since its simulated X-ray diffraction and Raman peaks are in excellent agreement with that obtained from experiments in [6]. In this work, we consider all the three reported cubic polytypes with an aim to understand from a fundamental point of view how differences in crystal structures correlate to their properties and to verify the suitability of available interatomic potentials for cubic BC_3.

Considering the interatomic potential, it is well known that for covalently bonded solids derived from the diamond structure, the Tersoff potential is the most appropriate one. The Tersoff potential was originally developed for C-based systems [25] and then it was modified for multicomponent systems to model heteronuclear bonds [26]. For B–C systems, two Tersoff potential parameters have been used thus far. The first one is by Matsunaga et al. [27], while the other by Kinaci et al. [28]. The Matsunaga potential has been used for simulating cubic boron carbonitride systems $C_x(BN)_{(1-x)}$ (x varies from 0–1) and it has successfully predicted the bulk modulus, lattice parameter and cohesive energy of these compounds. Matsunaga potential was used for MD simulations of BC_3 [24] and B_4C [29]. Kinaci potential has been used to predict thermal conductivity of hybrid graphene BN nanostructures. Kinaci et al. [28] have parameterized the Tersoff interaction to get ab-initio energetics of B–C and N–C bonds.

Since there are two potentials available for B and C systems, it is not clear, which of these potentials are well suited for BC_3. Therefore, the first step is to determine a suitable potential by analyzing the accuracy with which each of them predict certain basic properties. To this end, we use both the Matsunaga [27] and Kinaci potentials [28]. The B–B interaction we use is that of Matsunaga, since Kinaci parameterization does not consider these interactions. Once a suitable set of potential parameters is identified, other properties are determined using routine non-equilibrium MD and indentation simulations. Before proceeding, it is useful to consider a few works that have used nano-indentation experiments and simulations to understand various material properties.

Nanoindentation has been used to study various mechanical properties of the materials like hardness, dislocation source activation and phase transformation [30]. Mechanical properties like elastic modulus and hardness are routinely determined using Oliver-Pharr method [31]. Even MD simulations of indentations have provided useful insights concerning material behavior. For example, in [32] MD simulations were used to study the effect of temperature on dislocation activity beneath the indenter. It was found that, as the temperature increases, transition from elastic to plastic deformation occurs at progressively lower stresses. Arun et al. [33] have used MD to simulate nano-indentation studies of Ni thin films (both

single and polycrystalline Ni) and they found that low angle grain boundaries act as a source of dislocation under indenter. Cheng et al. [34] have also performed MD simulations to find the hardness of diamond (hard material) and gold (soft material) using Oliver-Pharr method and have reported that the hardness varies between 84–107 GPa and 5–7 GPa for diamond and gold, respectively. MD simulations of the indentation on iron carbides at various rates have helped conclude that Fe_3C is a harder material than Fe_4C [35]. For ceramic materials like Si, several interesting phenomena, such as phase transformation was found to occur on indentation [36]. Szlufarska et al. [37] performed nanoindentation using MD simulations on SiC and found that the crystalline to amorphous transformation of SiC occurred because of the coalescence of dislocation loops. Kucharski et al. [38] has used nanoindentation to determine the value of hardening index of 18G2A low-alloy steel and an aluminum alloy. In this manner, several insights can be obtained using MD simulations of indentation on materials.

SIMULATION DETAILS

All our simulations were conducted using the LAMMPS package [39], while Ovito [40] and VMD [41] were used for visualization purposes.

Structures of BC_3

The three models of cubic BC_3 (BC_3 (a), (b) and (c)) are shown in Figs. 1, *a–c*. The basic structures of BC_3 (a) and BC_3 (b) consist of a diamond cubic structure with two of the C atoms replaced by two B atoms at appropriate lattice points. BC_3 (c) is a 2×2×2 supercell having 64 atoms with 16 B atoms occupying the four principal diagonals as mentioned in [19]. One of the important features which distinguish the three structures is the extent of B–B bonding that is present in each structure. BC_3 (a) does not have any B–B bond, BC_3 (b) has one B–B bond within the unit cell while in BC_3 (c) all B atoms in the principal diagonals are bonded. For preparing the samples for MD simulations, the lattice parameter of BC_3 (a) is taken to be 3.601 Å (Table 2 of [24]) while that of BC_3 (b) is 3.685 Å (Table 1 of [12]) and for BC_3 (c) it is 7.330 Å as given in [19].

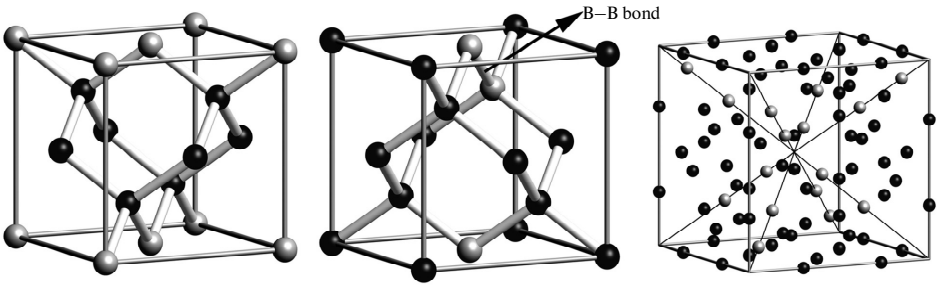

Fig. 1. Three cubic structures BC_3 (a), BC_3 (b) and BC_3 (c); atoms B are indicated using gray spheres, while black spheres indicate atoms C.

Simulation details – identification of the interatomic potential

For the determination of the interatomic potential, all the three BC_3 samples consisted of 8000 atoms (10×10×10 unit cells for BC_3 (a) and (b) 5×5×5 unit cells for BC_3 (c)) with periodic boundary conditions applied on three sides.

Lattice parameters, bulk modulus and cohesive energies were calculated using both the potentials and compared with available literature values to identify the

best potential. These simulations used a time step of 0.1 fs. For lattice parameter determination, the systems were relaxed to 300 K, 0 GPa using a combination of NVT and NPT ensembles. The first peak in the B–C radial distribution function was used to calculate the lattice parameter, which for BC_3 (a) and (b) structures are $\frac{\sqrt{3}}{4}a$, with a being the lattice constant. For BC_3 (c), the smallest distance between boron and carbon atoms corresponds to atoms at 8*c* (in principal diagonal) and 12*e* (at edge of super cell shared by four super cells of BC_3 (c)) positions, respectively, then that distance was used to calculate the lattice constant. For determining the bulk modulus, the simulation cell was equilibrated at 300 K and 0, 2.5, 5.0, 7.5 and 10.0 GPa pressures and the corresponding volumes were noted. The bulk modulus (B), was then calculated using the expression

$$B = -V\frac{dP^*}{dv}, \tag{1}$$

where V is the volume of the simulation cell while P^* is the pressure.

Simulation details – determination of the elastic constants

For a cubic structure, the non zero elastic constants (written in Voigt notation) are C_{11}, C_{12} and C_{44}. For the determination of elastic constants, two systems, each with 8000 and 64000 atoms were considered. The simulation cells were first equilibrated to 300 K using an NVT ensemble with a timestep of 0.1 fs for total time of 10 ps and then to 0 GPa and 300 K using an NPT ensemble with a time step of 0.1 fs for total time of 20 ps. After the equilibration, the length of all three sides of the simulation cell was the same, indicating that the potential predicts a cubic structure. To determine C_{11} and C_{12} tensile strain was applied on faces with normals in the X, Y or Z directions. When strain was applied on one of the faces (for example, the face normal to the X direction), the other two pairs of faces (those with Y and Z as the normals) were fixed. Strain was applied at a rate of 0.01 ps^{-1} for 2 ps resulting in a total strain of 0.02. The time step used in the simulation is 0.01 fs. For strain applied in the X direction, the simulation cell was constrained in the Y and Z directions. Then, using the constitutive Eqs. 2–4, C_{11} and C_{12} were determined. Similarly strain is applied in Y and Z directions keeping the other two sides fixed. Note that, for a tensile test in one direction, one value for C_{11} and two values for C_{12} are obtained:

$$\sigma_{xx} = C_{11}\varepsilon_{xx}; \tag{2}$$

$$\sigma_{yy} = C_{12}\varepsilon_{xx}; \tag{3}$$

$$\sigma_{zz} = C_{12}\varepsilon_{xx}. \tag{4}$$

For the determination of C_{44}, shear strains are applied in XY, YZ and XZ faces separately. When shear strain was applied on a face we have not constrained any of its sides and temperature was kept at 300 K. The strain rate used was 0.1 ps^{-1} and was applied for 0.2 ps with a time step of 0.1 fs resulting in a total shear strain of 0.02. For shear in XY face, C_{44} is calculated using the Eq. 5

$$\sigma_{xy} = C_{44}\gamma_{xy}. \tag{5}$$

C_{44} is also calculated by shearing YZ and XZ faces. The reported C_{11}, C_{12} and C_{44} are averages of three, six and three values, respectively.

Simulation details – determination of hardness

The number of atoms used for indentation was 2,56,000 with 40 unit cells in the *X* and *Z* directions and 20 unit cells in the Y direction for BC_3 (a) and (b). For BC_3 (c) 20×10×20 unit cells were used in the *X*, *Y* and *Z* directions, respectively. The simulation cell had the same dimensions as the sample in the *X* and *Z* directions, while it was 1000 Å in the *Y* direction. A schematic sketch of the simulation box used for indentation studies (not to scale) is shown in Fig. 2. Periodic boundary conditions are applied in all the three directions.

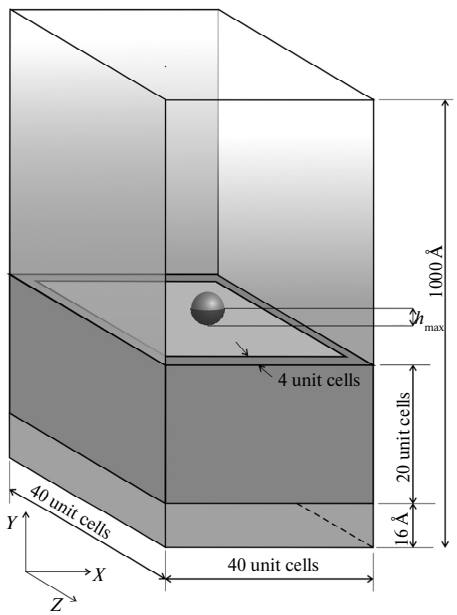

Fig. 2. Schematic of the simulation box used for the indentation (not to scale).

The system was equilibrated at 0 GPa and 300 K using NVT (for 10 ps) and then NPT (for 20 ps) ensembles with a time step of 0.1 fs. Atoms within a thickness of 4 unit cells in five of the six faces of the simulation cell were fixed while the sixth face was free and was indented. The indentation is carried out in the *Y*-direction at the center of *XZ* face at a rate of 0.01 Å/ps using a time step of 1 fs. The force exerted by the spherical indenter is given by Eq. 6. The force constant (*U*) used in the Eq. 6 was 1000 eV/Å^3, *r* is the distance from center of indenter to the each atom and *R* is radius of the indenter. The force that is applied is purely repulsive as in [42] and its value is zero when $r > R$. Arun et al. [33] has used the same repulsive force for conducting nanoindentation simulation on nickel thin films. We note that, the focus of this work is more on qualitative comparison of the three polytypes and the absolute value of *U* does not matter. The assumed value of *U* provided reasonable estimates of load-indentation depth (*P*–*h*) curves. After indentation, the hardness was obtained using Oliver-Pharr method [31] using Eqs. 7 and 8 given below:

$$Force = -U(r - R)^2, \text{ when } (r < R) \text{ and 0 other wise;} \quad (6)$$

$$h_c = h_{max} - 0.75(P_{max}/S_{max}); \quad (7)$$

$$Hardness = P_{max}/A_c, \quad (8)$$

where h_c is the contact depth based on which contact area A_c is calculated. P_{max} is the load at maximum depth h_{max}. S_{max} is the slope of the unloading curve at P_{max}. Simulations were carried out with four spherical indenters with radii 30, 45, 60 and 75 Å.

In order to obtain more reliable estimates of the hardness of the three materials, we also needed to determine the hardness using a different approach. To this end, the hardening index n of each material can be determined which can then be used to comment on the relative hardness of the materials as given in [38]. In an indentation test the *Mean Pressure* (i.e., hardness) is also given by

$$Mean\ Pressure = k(a/D)^n. \quad (9)$$

Here, k is a material constant, D is the diameter of the indenter, a is the radius of contact after indentation $\sqrt{Dh_c - hc^2}$ and n is a hardening index. It is to be noted that the *Mean pressure* physically represents the hardness (P/A_c) of the material. For studies involving the determination of the hardening index, unloading should be done from different points along the loading curve, since the hardness is obtained from the slope of the unloading curves at different maximum depths. Furthermore, these points are to be taken following plastic deformation of the material. The indentation studies performed in this work consumed significant computational time since we used really low indentation rates of 0.01 Å/ps to minimize strain rate effects as far as possible. Other works have used indentation rates which are at least one or two magnitudes higher [34], [37]. In order to minimize computational time, the hardness index determination was done only with indenter having 30 Å radius, since for this indenter size plasticity is reached for lower indentation depths. Unloading is done for three different depths for BC_3 (a), (b) and (c) and the corresponding *Mean Pressure* (analogous to stress) and *a/D* (analogous to strain) are calculated. The first unloading was done from a depth of 6.8, 6.9 and 6.2 Å for BC_3 (a), (b) and (c), while the second was done from a depth of 9.0, 8.9 and 8.0 Å for BC_3 (a), (b) and (c), respectively. The third unloading was done from 11.2, 10.8 and 9.7 Å for the three structures, respectively. The value of n was then found from the slope of log–log plot of Eq. 9.

RESULTS

Potential identification

The pressure showed a linear variation with volume for all the six cases (that is for the three structures using the two potentials). The comparison of lattice parameter, bulk modulus and cohesive energies are given in Tables 1, 2 and 3, respectively. The Ref. [24] gives MD values while Refs. [12] and [19] correspond to ab-initio values.

It is seen that the lattice parameter predicted by the Matsunaga potential are closer to the literature values, for all the three structures. However, the values obtained from the Kinaci potential are only slightly higher. As far as the bulk modulus is concerned, the Kinaci potential seems to be more accurate, while Matsunaga over predicts the values. However, when we consider the cohesive energies, it is very clear that the Matsunaga potential is closer to ab-initio values, when compared to the Kinaci potential. It is to be noted that, when compared to ab-initio values, the cohesive energies are high even for Matsunaga potential by approximately 1.1 eV/atom for BC_3 (a) and (b). For BC_3 (c), the absolute values of the cohesive energy and bulk modulus were not available and is hence not reported.

Nonetheless, the lattice parameters for BC_3 (c) show a good agreement with the literature values as shown in Table 1.

Table 1. Lattice parameter, Å

Structure	Matsunaga	Kinaci	Literature
BC_3 (a)	3.6543	3.7707	3.601 [24]
BC_3 (b)	3.6155	3.7804	3.685 [12]
BC_3 (c)	7.2105	7.4400	7.330 [19]

Table 2. Bulk modulus, GPa

Structure	Matsunaga	Kinaci	Literature
BC_3 (a)	361.39	344.29	342 [24]
BC_3 (b)	357.96	331.27	337 [12]
BC_3 (c)	355.60	332.91	–

Table 3. Cohesive energy, eV/atom, taken from [12]

Structure	Matsunaga	Kinaci	Literature
BC_3 (a)	–7.2064	–5.8261	–9.265 (LDA)
			–8.307 (GGA)
BC_3 (b)	–7.1318	–5.9476	–9.176 (LDA)
			–8.281 (GGA)
BC_3 (c)	–7.1353	–5.9540	–

From this preliminary analysis, it is clear that the both potentials are reasonable as far as the bulk modulus and the lattice parameters are concerned. The cohesive energies are however still much higher than what is predicted by ab-initio calculations, with Matsunaga parameters showing lower values. Therefore, in what is to follow, we will use the Matsunaga parametrized Tersoff potential for further studies. It is however important that a better parametrization of the potential is probably needed so that the cohesive energies are better predicted, which is left for future research.

Elastic constants

For all the three structures, the stress was proportional to the strain. The calculated values of C_{11}, C_{12} and C_{44} are averaged over the values obtained from simulations performed in each of the three directions and are given in Tables 4, 5 and 6, respectively along with the standard deviations. It is seen that the calculated value of elastic constants are in close agreement with the literature value [24], which were also computed using MD simulations. Furthermore, it can be seen that the sizes of the simulation cell does not affect the values significantly, confirming that the values have converged with respect to simulation box sizes. The values predicted for BC_3 (c) are higher than what is predicted by ab-initio calculations, by 14 %.

The effective isotropic bulk modulus (B'), shear modulus (G), Young's modulus (E) and Poisson's ratio (v) are obtained for the three structures and given in Table 7. Considering the Young's modulus and the shear modulus, BC_3 (a) seems to be stiffer than the other two. One possible reason for the lower stiffness of BC_3 (b) and (c) when compared to BC_3 (a) seems to be the presence of weaker B–B bonding in BC_3 (b) and (c).

Table 4. Average value of C_{11}, GPa, for BC_3 (a), (b) and (c) with standard deviation given in parenthesis

Structure	8000 atoms	64000 atoms	Literature
BC_3 (a)	762.13 (36.92)	761.52 (37.21)	759 [24]
BC_3 (b)	744.11 (6.75)	743.26 (0.72)	–
BC_3 (c)	751.85 (2.06)	739.30 (1.04)	658.4 [19]

Table 5. Average value of C_{12}, GPa, for BC_3 (a), (b) and (c) with standard deviation given in parenthesis

Structure	8000 atoms	64000 atoms	Literature
BC_3 (a)	100.76 (8.40)	101.42 (8.52)	116 [24]
BC_3 (b)	105.83 (1.29)	109.00 (1.67)	–
BC_3 (c)	104.17 (1.29)	106.75 (2.93)	194.7 [19]

Table 6. Average value of C_{44}, GPa, for BC_3 (a), (b) and (c) with standard deviation given in parenthesis

Structure	8000 atoms	64000 atoms	Literature
BC_3 (a)	468.40 (16.98)	465.64 (18.29)	483 [24]
BC_3 (b)	416.32 (9.43)	416.64 (0.27)	–
BC_3 (c)	423.57 (9.72)	425.82 (1.12)	392.5 [19]

Table 7. Isotropic properties for three structures

Structure	B', GPa	G, GPa	E, GPa	v
BC_3 (a)	321.45	411.40	865.00	0.0514
BC_3 (b)	320.42	376.84	812.14	0.0776
BC_3 (c)	321.78	384.51	824.94	0.0727

Indentation studies

Nature of the load-indentation depth curves. So far indentation studies have not been performed for BC_3 structures using MD simulations. In this paper, nano-indentation simulations are carried out on BC_3 structures to understand the differences in mechanical properties between the three polytypes and to understand their response to local plastic deformation. Four different indenter radii are used as mentioned in Section 2.4. The P–h curves of all three BC_3 structures with the four indenters are shown in Figs. 3–6. It is seen that, for all three structures, and for all the indenter sizes a drop in the load occurs at a certain indentation depth. Further, the drop seems to occur at higher depths for BC_3 (b), followed by BC_3 (a) and then BC_3 (c). This drop in the load is associated with the onset of plastic deformation. Clearly, BC_3 (c) seems to have lower yield/failure limit when compared to the other two materials. The extent of the drop also qualitatively decreases with increase in indenter size. In particular, for BC_3 (c), indentations performed with 75 Å indenter size (see Fig. 6), almost show no drop. Instead, a flat region can be seen (shown in the figure) suggesting a more gradual flow of the material as seen in a perfectly plastic material.

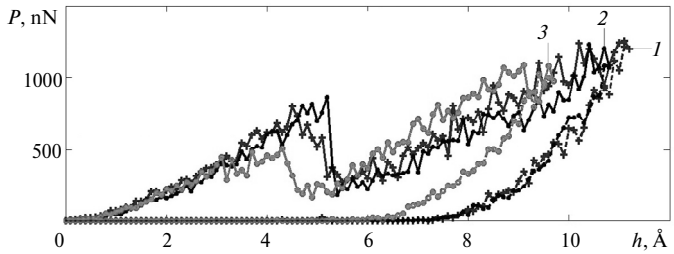

Fig. 3. Load vs. depth for three structures using 30 Å radius indenter; *1*, *2* and *3* represent BC_3 (a), (b) and (c), respectively.

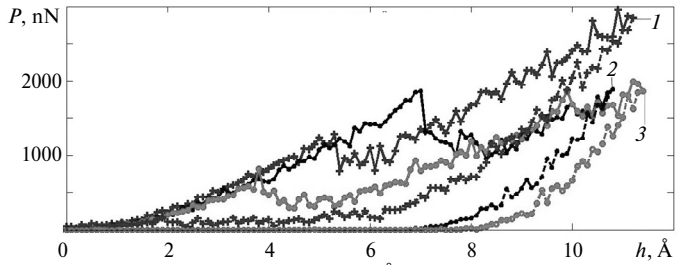

Fig. 4. Load vs. depth for three structures using 45 Å radius indenter; *1*, *2* and *3* represent BC_3 (a), (b) and (c), respectively.

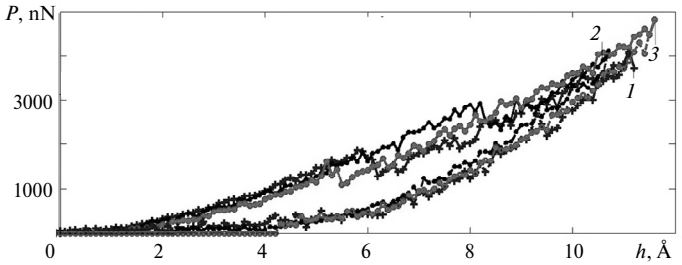

Fig. 5. Load vs. depth for three structures using 60 Å radius indenter; *1*, *2* and *3* represent BC_3 (a), (b) and (c), respectively.

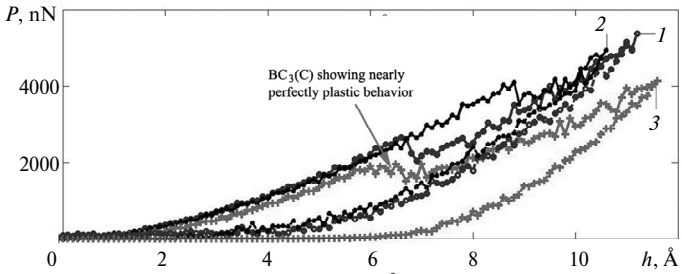

Fig. 6. Load vs. depth for three structures using 75 Å radius indenter; *1*, *2* and *3* represent BC_3 (a), (b) and (c), respectively.

On examining the unloading portions of the *P–h* curves, it is seen that permanent indentation left in the material, following retraction of the indenter, depends on the material as well as the indenter size. For 30 Å, BC_3 (a) and (b) seem to show more or less a similar permanent deformation, while BC_3 (c) shows greater elastic recovery. For 45 Å, BC_3 (b) shows a larger permanent plastic deformation when compared to BC_3 (c). In this case, BC_3 (a), seems to show no permanent indentation. For 60 Å none of the material shows a permanent deformation, while for 75 Å, only BC_3 (c) shows permanent depth. Since the loading portion of the curve

shows a drop in the load (indicating some dissipation due to plastic deformation), the unloading curve is expected to show some permanent depth due to indentation. The lack of a permanent indentation in the *P–h* curves following unloading, despite the dissipative effects seen on loading prompted us to examine the indentation processes more closely. In Figs. 7, *a–h*, the BC_3 (a) sample on complete indentation (*a*, *c*, *e* and *g*), and after complete unloading (*b*, *d*, *f* and *h*) for all four radii are shown. It is seen that, for 30 Å radius, on indentation a certain amount of pile-up of the material occurs (see Fig. 7, *a*), while on complete unloading, this pile-up is more or less preserved and a permanent indentation is present (see Fig. 7, *b*). For the 45 Å radius, we see that, on indentation no pile-up occurs (see Fig. 7, *c*), while on complete unloading, some amount of pile-up occurs (see Fig. 7, *d*). The 60 Å and the 75 Å simulations also show a similar behavior. In fact, for these indenter radii, it appears as if the material has fully recovered back to its initial configuration. The depth (*h*) is measured between the center of the indenter and the surface of the sample. Since the material rises along with the indenter for the 45, 60 and the 75 Å cases, it appears as though the material fully recovers (with no permanent indentation) in the *P–h* diagram (see Figs. 4–6). Thus it can be concluded that, for those simulations where the indentation produced pile-up, a permanent depth was seen on unloading. If the simulation did not produce pile-up on indentation, then a pile-up of the material was observed on unloading. This happened to be the case for BC_3 (b) as well. Namely, no pile-up was seen for 60 and 75 Å on indentation, and unloading did not show a permanent depth in the *P–h* curve (see Figs. 5 and 6). Both BC_3 (a) and BC_3 (b) seemed to show a trend in their behavior, i.e., lower indenter sizes (30 Å for BC_3 (a), 30 and 45 Å for BC_3 (b)) showed a pile-up on indentation and hence a permanent depth in the *P–h* curve. Furthermore, as the indenter sizes were increased they did not show pile-up during indentation and instead the material was found to rise up producing material pile-up on unloading. For BC_3 (c), an anomalous behavior was observed where the 30, 45, and 75 Å showed a pile-up on indentation, while the 60 Å did not. We rerun our simulations for 60 Å (BC_3 (c)) to check the correctness of our simulation but did not find any specific errors which could have caused this anomalous behavior. Hence, at this point we are not sure of the exact reason for this anomaly in BC_3 (c).

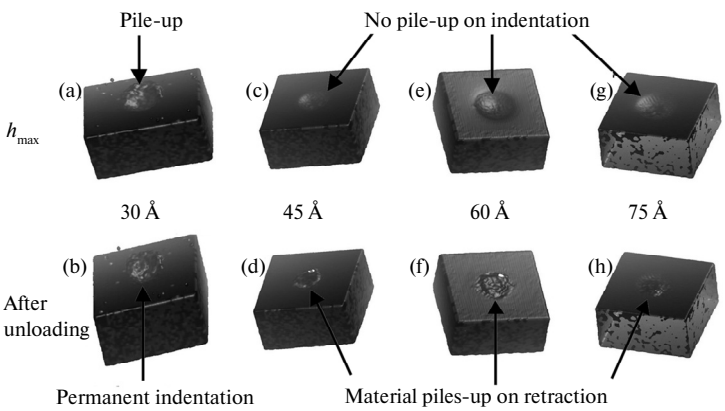

Fig. 7. The surface of BC_3 (a) at h_{max} and after unloading.

In order to understand the reason behind the rising up of the material, during unloading, the nature of the material beneath the indenter was examined. In particular, a cylindrical region was considered beneath the indented portion and the

total radial distribution function $g(r)$ was plotted for all three materials before and after the indentation. The cylinder was 20 Å in radius and had a depth of 12 Å with its axis parallel to the *Y*-axis (in direction of loading). The center of the top of the cylinder was on *XZ* plane, where the indenter initially touches the sample. Fig. 8 shows $g(r)$ for BC_3 (a), (b) and (c) before loading, at h_{max} and after unloading. Results from the 75 Å indenter radius is used here for illustration, all the radii showed the same behavior. For all the three materials, it can be seen that the peaks which are present before the simulations vanish after the indentation. Clearly, the process of indentation amorphizes the material beneath the indenter.

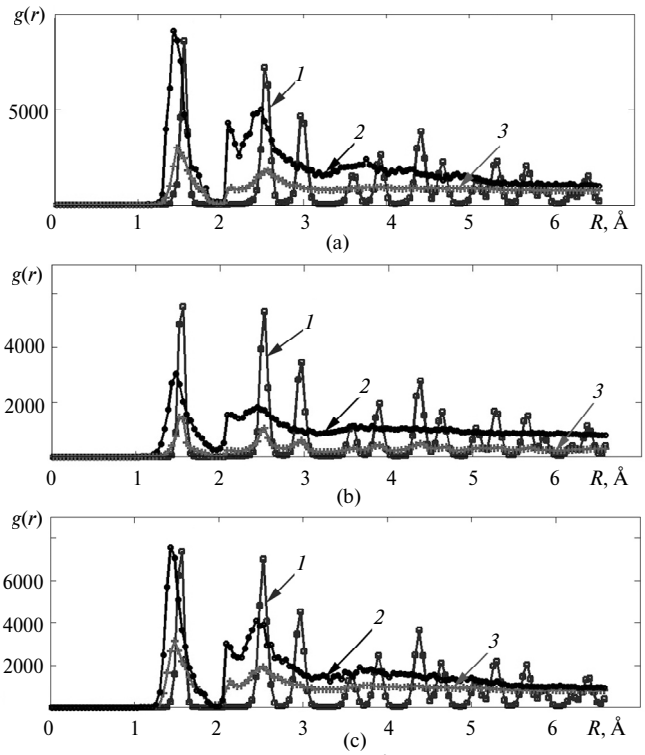

Fig. 8. RDF of BC_3 (a), (b) and (c) indenter radius 75 Å; *1*, *2* and *3* represent RDF before loading, h_{max} and after loading, respectively.

One hypothesis due to which the material might pile-up during unloading is if the amorphous material occupied more volume than its crystalline counterpart. This increase in volume would cause the amorphous material to occupy more space, which would be available only when the indenter is withdrawn. To check this hypothesis, samples of the three materials with 8000 atoms (10×10×10 unit cells) was amorphized using MD by increasing the temperature to 6500 K and then quenching it to 0 GPa and 300 K in an NPT ensemble allowing the volume to relax. The results of average volume (standard deviations associated with all the volumes were less than 0.25 %) for the three structures are tabulated in Table 8. It is very clear that the amorphous material occupies nearly 40 % more volume than its crystalline counterpart, for all the three materials considered. Hence, we conclude that for BC_3 (a) (with indenter radius 30 Å) and BC_3 (b) (with indenter radius 30 and 45 Å) pile-up occurs during indentation thus removing some material. On removal of load, the amorphized material had additional space to occupy due to which a certain permanent depth was seen. However, for higher radii, indentation

did not produce any pile-up and the amorphous material was trapped within the material. So, when the indenter was withdrawn, it caused the amorphized material to rise up. A similar physics is also true for BC_3 (c), except that there is no clear trend with indenter radii.

Table 8. Volume, Å^3, at 300 K and 0 GPa in crystalline and amorphous state

Structure	Crystalline	Amorphous	% Difference
BC_3 (a)	47167.89	65845.45	39.6
BC_3 (b)	46931.71	65846.85	40.3
BC_3 (c)	46993.52	65249.56	38.9

Hardness. The Table 9 shows the hardness value as determined by the Oliver-Pharr method and the depth at which plasticity onsets (given in parentheses). The depth to reach the plastic state was identified from the first major drop observed in the *P–h* curves (see Figs. 3–6). As expected, the indentation depth required to reach plastic state increases with the indenter size. This variation occurs because, at given depth, the stress induced by larger indenter will be lower than what is induced by the smaller indenter. The hardness value also seems to increase with indenter radius for BC_3 (a) and (b), while for BC_3 (c), the 60 Å shows higher hardness than 75 Å. It is important to note that the hardness values determined here are for comparative purposes only. The Oliver-Pharr method is known to over predict the hardness values due to the presence of pile-up. The over prediction of the hardness is due to the fact that the A_c calculated will be less than the actual value if pile-up is present [43]. Since the extent of over prediction is difficult to estimate, the hardness comparisons between the three structures can be made only for indenter sizes, where there was no pile-up on indentation. However, the difference in the hardness between BC_3 (a) and (b) is not significant enough to clearly assert that BC_3 (b) is harder than (a). For BC_3 (c), the 60 Å case did not show any pile-up on indentation and the hardness value indicates that both BC_3 (a) and (b) are softer than BC_3 (c). In contrary, the *P–h* curves (see Figs. 3–6), suggest that BC_3 (c) is softer, with lower magnitudes of load drops during loading. Therefore, the hardness determination using Oliver-Pharr method in this case does not seem to be conclusive. In order to confirm the trend in the hardness between BC_3 (a) and BC_3 (b) and to ensure that BC_3 (c) indeed has the least hardness, the hardening index of the three materials are examined.

Table 9. Hardness, GPa, and depth, Å, (number in parenthesis) at which plasticity begins

Structure	Indenter radius, Å			
	30	45	60	75
BC_3 (a)	83 (4.6)	132 (5.3)	138 (6.1)	136 (6.7)
BC_3 (b)	77 (4.9)	79 (5.3)	141 (8.2)	141 (8.8)
BC_3 (c)	79 (4.3)	70 (5.2)	149 (5.2)	99 (6.0)

Determination of hardening index and their comparisons. Figure 9 shows *P–h* curves for the three BC_3 structures after they are unloaded from three different depths. Figure 10 shows the variation of log (*Mean Pressure*) with log(*a/D*) from which the hardening index *n* was calculated using Eq. 9. In this plot, the labeled

points for each material indicates the depths from which unloading was carried out. The values of n for each portion are tabulated in Table 10. Clearly, the material's resistance to plastic deformation reduces with indentation depth. For example, for BC_3 (c), the line connecting points (3a) and (3b) has a slope of 4.98, while that connecting (3b) and (3c) has a slope of 0.3.

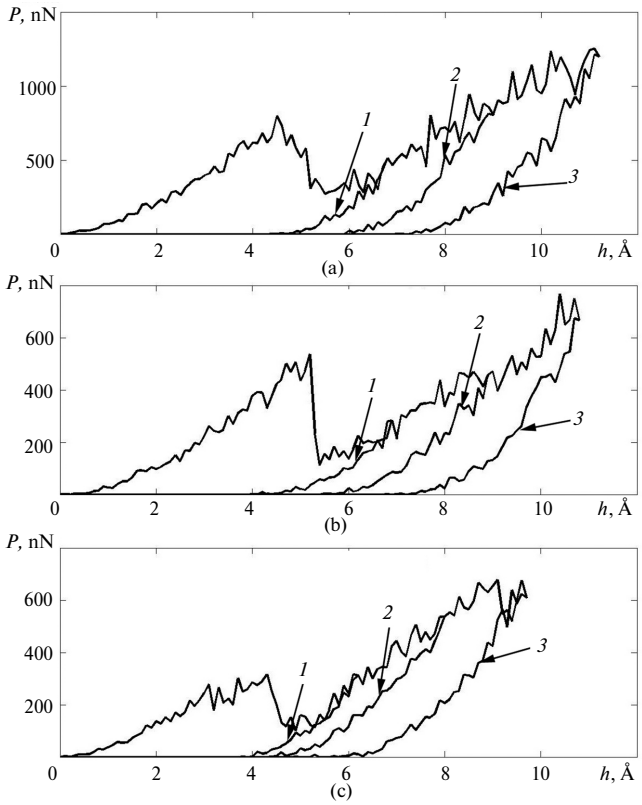

Fig. 9. Load vs. depth for three structures at different depths for the three structures BC_3 (a), (b) and (c); *1*, *2* and *3* represent unloading curves at first, second and third (deepest) depth, respectively.

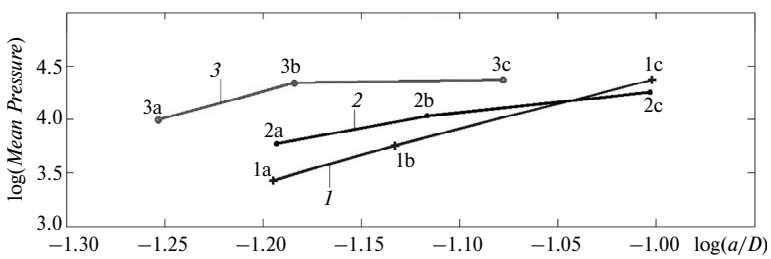

Fig. 10. log(*Mean Pressure*) vs. log(a/D) for the three BC_3 structures; *1*, *2* and *3* represent BC_3 (a), (b) and (c), respectively; the three points a, b and c represent unloading at three different depths.

If we consider the values of hardening index, it is clear that BC_3 (a) is harder than BC_3 (b) or (c). However, considering lower indentation depths, BC_3 (c) is harder than BC_3 (b), while for higher depths, BC_3 (c) is the softest. Hence, it can be concluded that the hardness depends on the indentation depth and the kind of plastic mechanisms which are triggered at different depths.

Table 10. The hardening index of the three structures

Structure	Hardening Index-Part 1	Hardening Index-Part 2
BC_3 (a)	5.29	4.66
BC_3 (b)	3.31	1.38
BC_3 (c)	4.98	0.30

The contact area, A_c used to predict the hardness is less than the actual value if pile-up is there [44]. The variation of number of atoms that are piled-up during indentation is shown in Fig. 11. The number of atoms getting piled up are maximum for BC_3 (c), followed by (b) and then by (a) for the same depth. If the pile-up is more, then the contact area predicted will be less than the actual value. The atoms begin to pile-up much before elastic state is reached in case of BC_3 (c) but for (a) and (b) pile-up begins just after it has crossed elastic limit. The structure which shows highest tendency to pile-up will have low strain hardening index [45]. Furthermore, to examine the ease with which the damage/plastic deformation produced as indentation proceeds, the number of atoms dislocated is plotted in Fig. 12. Those atoms whose coordination number is different from bulk atoms are dislocated atoms [46]. For the calculations of number of dislocated atoms, we have considered only bulk atoms (not the surface atoms). Clearly, for BC_3 (a) there is a burst in the number of dislocated atoms, at around 5 Å depth, after which this value increases slowly with increase in depth. For BC_3 (b), the burst in the activity beneath the indenter is more gradual and it also continues to increase with depth. For, BC_3 (c), the onset of plasticity occurs much earlier and then continues to increase with depth as for BC_3 (b) but at a much higher rate. These plots clearly show that, BC_3 (c) has a more ductile behavior than BC_3 (b). BC_3 (a) seems to be more brittle. This difference is probably due to the B–B bonding present in BC_3 (b) and BC_3 (c) which is absent in BC_3 (a) as suggested in [19].

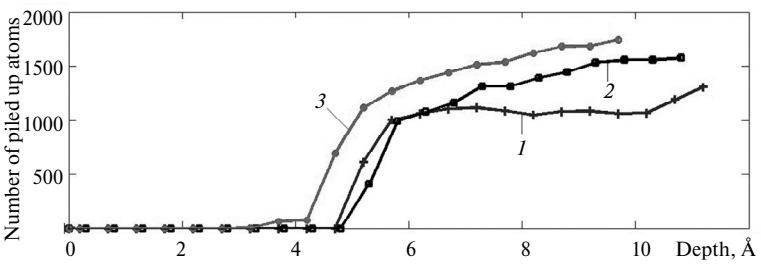

Fig. 11. Variation of number of piled-up atoms for the three BC_3 structures using 30 Å indenter radius; *1*, *2* and *3* represent BC_3 (a), (b) and (c), respectively.

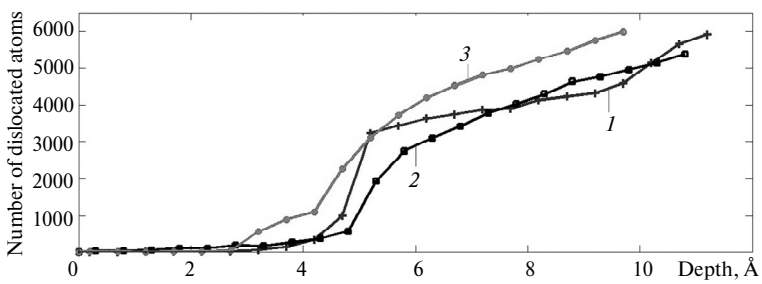

Fig. 12. Variation of number of defects with depth for three BC_3 structures; *1*, *2* and *3* represent BC_3 (a), (b) and (c), respectively.

CONCLUSIONS

Among the available potentials for BC_3, the Tersoff potential as parameterized by Matsunaga [27] seems to be more appropriate. Even though the elastic properties were predicted accurately when compared to existing ab-initio values, the cohesive energies of Matsunaga showed a difference of close to 1.1 eV/atom when compared to ab-initio values for BC_3 (a) and (b). This discrepancy might have arised due to the fact that the B–C and B–B parameters were not explicitly fit to reproduce properties of BC_3. For BC_3 (c), the absolute value of energy is not reported in the literature [19] but the lattice parameter and elastic constants showed good agreement with the literature values.

With regard to response to indentation, the *P–h* curves seemed to suggest that BC_3 (c) showed lower yield strength (hence lower hardness). Furthermore, the post yield behavior was also less stiff for BC_3 (c) when compared to the other two structures. For example, the 45 and 75 Å indenter radii generated *P–h* curves showed significant ductility for BC_3. This behavior is probably due to the breaking of the B–C and then B–B bonds along the weak <111> direction, which is in accordance with [19].

The indentation studies also pointed to a peculiar "pile-up on retraction" behavior when larger indenter radii were used. This behavior points to the fact that the material underneath the indenter gets amorphized under pressure. Amorphization during nanoindentation is seen for several materials like Fe_3C, Fe_4C [35] and SiC [37] but has not been shown for BC_3.

The tendency to pile-up increases with the number of B–B bonding. So here the tendency was maximum for BC_3 (c) followed by BC_3 (b) and then by BC_3 (a). The hardness predicted by Oliver-Pharr method increases with decrease in value of A_c. This hardness was inconclusive and suggested almost identical hardness for all the three polytypes. A more detailed study based on the hardness index revealed that the hardness depended on the depth of indentation. The resistance to plastic deformation decreases with increase in depth as more atoms are dislocated and hence unable to resist the deformation.

ACKNOWLEDGEMENT

Authors are grateful to the computing facility at P G Senapathy Center for Computing Resource, IIT Madras. The computation was done in Virgo super cluster.

Методом молекулярної динаміки проведено моделювання механічних властивостей і твердості трьох політипів кубічного BC_3 та їх порівняння. Для системи бор–вуглець з літературних даних ідентифіковано два міжатомних потенціалу Терсоффа з різними параметрами. На основі існуючих ab-initio досліджень енергії когезії і структурних властивостей проаналізовано придатність цих двох потенціалів для прогнозування властивостей BC_3. З використанням кращого міжатомного потенціалу більш детальне моделювання методом молекулярної динаміки виконано для оцінки та порівняння пружності, плинності, пост-плинної поведінки і твердості трьох політипів BC_3. Значення констант пружності добре узгоджуються з існуючими їх значеннями ab-initio для трьох політипів і відрізняються один від одного не більше ніж на 15 %. Реакція на індентування має значні якісні відмінності під час занурення індентора та під час розвантаження. Один з політипів має меншу межу плинності і здається більш пластичним, ніж два інших. Твердість також має складну залежність як від матеріалу, так і від глибини занурення індентора. Також спостерігали своєрідну залежність виникнення навалів від розміру індентора. Зокрема, за меншим радіусом індентора спостерігали виникнення навалів біля відбитка під час занурення індетнора. При збільшенні радіуса індентора виникнення навалів спостерігали тільки при розвантаженні індентора.

Більший об'єм, що займає аморфізований матеріал, який формується під час індентування, виявився причиною виникнення навалів при розвантаженні індентора.

***Ключові слова**: надтверді матеріали, константи пружності, твердість, молекулярна динаміка, легований бором алмаз.*

Методом молекулярной динамики проведено моделирование механических свойств и твердости трех политипов кубического BC_3 и их сравнения. Для системы бор–углерод по литературным данным идентифицировано два межатомных потенциала Терсоффа с различными параметрами. На основе существующих ab-initio исследований энергий когезии и структурных свойств проанализирована пригодность этих двух потенциалов для прогнозирования свойств BC_3. С использованием лучшего межатомного потенциала более детальное моделирование методом молекулярной динамики выполнено для оценки и сравнения упругости, текучести, пост-текучего поведения и твердости трех политипов BC_3. Значение констант упругости хорошо согласуются с существующими их значениями ab-initio для трех политипов и отличаются друг от друга не более чем на 15 %. Реакция на индентирования имеет значительные качественные различия во время погружения индентора и во время разгрузки. Один из политипов имеет меньший предел текучести и кажется более пластичным, чем два других. Твердость также имеет сложную зависимость как от материала, так и от глубины погружения индентора. Также наблюдали своеобразную зависимость возникновения навалов от размера индентора. В частности, при меньшему радиусе индентора наблюдали возникновение навалов у отпечатка во время погружения индетнора. При увеличении радиуса индентора возникновения навалов наблюдали только при разгрузке индентора. Больший объем, что занимает аморфизированный материал, который формируется во время индентирования, оказался причиной возникновения навалов при разгрузке индентора.

***Ключевые слова**: сверхтвердые материалы, константы упругости, твердость, молекулярная динамика, легированный бором алмаз.*

1. Veprek S. The search for novel, superhard materials. *J. Vacuum Sci. & Tech.* A. 1999. Vol. 17, no. 5. P. 2401–2420.
2. Oganov A.R., Solozhenko V.L. Boron: a hunt for superhard polymorphs. *J. Superhard Mater.* 2009. Vol. 31, no. 5. P. 285–291.
3. He D., Zhao Y., Daemen L., Qian J., Shen T., Zerda T. Boron suboxide: As hard as cubic boron nitride. *Appl. Phys. Lett*. 2002. Vol. 81, no. 4. P. 643–645.
4. Wentorf R., Jr. Synthesis of the cubic form of boron nitride. *J. Chem Phys.* 1961. Vol. 34, no. 3. P. 809–812.
5. Zhao Y., He D., Daemen L., Shen T., Schwarz R., Zhu Y., Bish D., Huang J., Zhang, J., Shen G. et al. Superhard B–C–N materials synthesized in nanostructured bulks. *J. Mater. Res.* 2002. Vol. 17, no. 12. P. 3139–3145.
6. Zinin P., Ming L., Ishii H., Jia R., Acosta T., Hellebrand E. Phase transition in BC_x system under high-pressure and high-temperature: Synthesis of cubic dense BC_3 nanostructured phase. *J. Appl. Phys.* 2012. Vol. 111, no. 11. art. 114905.
7. Solozhenko V. L., Kurakevych O. O., Andrault D., Le Godec Y., Mezouar M. Ultimate metastable solubility of boron in diamond: synthesis of superhard diamondlike BC_5, *Phys. Rev. Lett.*, 2009, Vol. 102, no. 1, art. 015506.
8. Crowther, P., Dean, P., and Sherman, W., Excitation spectrum of aluminum acceptors in diamond under uniaxial stress. *Phys. Rev.* 1967. Vol. 154, no. 3. P. 772–785.
9. Ekimov E., Sidorov V., Bauer E., Mel'nik N., Curro N., Thompson, J., Stishov S. Superconductivity in diamond. *Nature*. 2004. Vol. 428, no. 6982. P. 542–545.
10. Swain G. M., Ramesham R. The electrochemical activity of boron-doped polycrystalline diamond thin film electrodes. *Anal. Chem.* 1993. Vol. 65, no. 4. P. 345–351.
11. Mikhaylushkin A.S., Zhang X., Zunger A. Crystal structures and metastability of carbon-boron compounds C_3B and C_5B. *Phys. Rev. B*. 2013. Vol. 87, no. 9, art. 094103.
12. Lowther J.E. Potential super-hard phases and the stability of diamond-like boron–carbon structures. *J. Phys.*: *Condens. Matter.* 2005. Vol. 17, no. 21. P. 3221–3229.
13. Liu Z., He J., Yang J., Guo X., Sun H., Wang H.-T., Wu E., Tian Y. Prediction of a sandwichlike conducting superhard boron carbide: First-principles calculations. *Phys. Rev. B*. 2006. Vol. 73, no. 17, art. 172101.

14. Liu H., Li Q., Zhu L., Ma Y. Superhard and superconductive polymorphs of diamond-like BC_3. *Phys. Lett. A*. 2011. Vol. 375, no. 3. P. 771–774.
15. Ma M., Yang B., Li Z., Hu M., Wang Q., Cui L., Yu D., He J. A metallic superhard boron carbide: first-principles calculations. *Phys. Chem. Chem. Phys.* 2015. Vol. 17. P. 9748–9751.
16. Li Q., Wang H., Tian Y., Xia Y., Cui T., He J., Ma Y., Zou G. Superhard and superconducting structures of BC_5. *J. Appl. Phys*. 2010. vol. 108, art. 023507.
17. Liang Y., Zhang W., Zhao J., Chen L. Super hardness, stability, and metallicity of diamond-like BC_5: density functional calculations. *Phys. Rev. B*. 2009. Vol. 80, no. 11. art. 113401.
18. Lazar P., Podloucky R. Mechanical properties of superhard BC_5, *Appl. Phys. Lett.*, 2009. Vol. 94, no. 25, art. 251904.
19. Zhang M., Liu H., Li Q., Gao B., Wang Y., Li H., Chen C., Ma Y. Superhard BC_3 in cubic diamond structure. *Phys. Rev. Lett.* 2015. Vol. 114, no. 1, art. 015502.
20. Yan Q., Wang B., Wang Y.X., Yang J., Yang G. et al. Predicted boron-carbide compounds: A first-principles study. *J. Chem. Phys*. 2014. Vol. 140, no. 22, art. 224704.
21. Yang J., Sun H., He J., Tian Y., Chen C. Diamond-like BC_3 as a superhard conductor identified by ideal strength calculations. *J. Phys.: Condens. Matter.* 2007. Vol. 34, no. 19, art. 346223.
22. Du X., Zhao H., Zhang L., Yang Y., Xu H., Fu H., Li L. Molecular dynamics investigations of mechanical behaviours in monocrystalline silicon due to nanoindentation at cryogenic temperatures and room temperature. *Sci. Rep.* 2015. Vol. 5, art. 16275.
23. Swaminathan N., Kamenski P. J., Morgan D., Szlufarska I. Effects of grain size and grain boundaries on defect production in nanocrystalline 3C–SiC. *Acta Mater.* 2010. Vol. 58, no. 8. P. 2843–2853.
24. Nkambule S.M., Lowther J. Crystalline and random diamond-like boron-carbon structures. *Solid State Commun.* 2010. Vol. 150, no. 1. P. 133–136.
25. Tersoff J. Empirical interatomic potential for carbon, with applications to amorphous carbon. *Phys. Rev. Lett.* 1988. Vol. 61, no. 25. P. 2879.
26. Tersoff J. Modeling solid-state chemistry: interatomic potentials for multicomponent systems. *Phys. Rev. B*. 1989. Vol. 39, no. 8. P. 5566–5568.
27. Matsunaga K., Fisher C., Matsubara H. Tersoff potential parameters for simulating cubic boron carbonitrides. *Jap. J. Appl. Phys.* 2000. Vol. 39, Pt. 2, no. 1A/B. P. L48–L51.
28. Kinaci A., Haskins J. B., Sevik C., Cagin T. Thermal conductivity of BN–C nanostructures. *Phys. Rev. B*. 2012. Vol. 86, no. 11, art. 115410.
29. Letsoalo T., Lowther J. Elastic and thermodynamic properties of potentially superhard carbon boride materials. *J. Superhard Mater.* 2012. Vol. 34, no. 1. P. 28–36.
30. Schuh C. A. Nanoindentation studies of materials. *Mater. Today*. 2006. Vol. 9, no. 5. P. 32–40.
31. Oliver W.C., Pharr G.M. An improved technique for determining hardness and elastic modulus using load and displacement sensing indentation experiments. *J. Mater. Res*. 1992. Vol. 7, no. 6. P. 1564–1583.
32. Lund A.C., Hodge A. M., Schuh C. A. Incipient plasticity during nanoindentation at elevated temperatures. *Appl. Phys. Lett.* 2004. Vol. 85, no. 8. P. 1362–1364.
33. Nair A. K., Parker E., Gaudreau P., Farkas D., Kriz R.D. Size effects in indentation response of thin films at the nanoscale: A molecular dynamics study. *Int. J. Plasticity*. 2008. Vol. 24, no. 11. P. 2016–2031.
34. Liu C.-L., Fang T.-H., Lin J.-F. Atomistic simulations of hard and soft films under nanoindentation. *Mater. Sci. Eng.* A. 2007. Vol. 452. P. 135–141.
35. Goel S., Joshi S.S., Abdelal G., Agrawal A. Molecular dynamics simulation of nano- indentation of Fe_3C and Fe_4C. *Mater. Sci. Eng.* A. 2014. Vol. 597. P. 331–341.
36. Jang J.-I., Lance M., Wen S., Tsui T. Y., Pharr G. Indentation-induced phase transformations in silicon: influences of load, rate and indenter angle on the transformation behavior. *Acta Mater.* 2005. Vol. 53, no. 6. P. 1759–1770.
37. Szlufarska I., Kalia R.K., Nakano A., Vashishta P. Nanoindentation induced amorphization in silicon carbide. *Appl. Phys. Lett.* 2004. Vol. 85, no. 3. P. 378–380.
38. Kucharski S., Mroz Z. Identification of plastic hardening parameters of metals from spherical indentation tests. *Mater. Sci. Eng.* 2001. Vol. A 318, no. 1. P. 65–76.
39. Plimpton S. Fast parallel algorithms for short-range molecular dynamics. *J. Comput. Phys.* 1995. Vol. 117, no. 1. P. 1–19.
40. Stukowski A. Visualization and analysis of atomistic simulation data with ovito {the open visualization tool}. *Model. Simul. Mater. Sci. Eng.* 2009. Vol. 18, no. 1, art. 015012.

41. Humphrey W., Dalke A., Schulten K. VMD: visual molecular dynamics. *J. Mol. Graph.* 1996. Vol. 14, no. 1. P. 33–38.
42. Kelchner C. L., Plimpton S., Hamilton J. Dislocation nucleation and defect structure during surface indentation. *Phys. Rev. B*. 1998. Vol. 58, no. 17. P. 11085–11088.
43. Mulford, R., Asaro, R. J., and Sebring, R.J., Spherical indentation of ductile power law materials. *J. Mater. Res.* 2004. Vol. 19, no. 9. P. 2641–2649.
44. Bolshakov A., Pharr G. Influences of pileup on the measurement of mechanical properties by load and depth sensing indentation techniques. *J. Mater. Res.* 1998. Vol. 13, no. 4. P. 1049–1058.
45. Alcala J., Giannakopoulos A., Suresh S. Continuous measurements of load-penetration curves with spherical micro indenters and the estimation of mechanical properties. *J. Mater. Res.* 1998. Vol. 13, no. 5. P. 1390–1400.
46. Li D., Wang F., Yang Z., Zhao Y. How to identify dislocations in molecular dynamics simulations? *Sci. China Phys. Mech. Astron.* 2014. Vol. 57, no. 12. P. 2177–2187.

Received 25.09.17
Revised 09.01.18
Accepted 09.01.18